

A study of Be stars in the time domain

I. Spectral data and polarimetry

A. Castaⁿón Esteban,¹* I.A. Steele,¹ H. Jermak¹

¹*Astrophysics Research Institute, Liverpool John Moores University, 146 Brownlow Hill, Liverpool L3 5RF, UK*

Accepted XXX. Received YYY; in original form ZZZ

ABSTRACT

We present the first part of a spectroscopic and polarimetric study on a sample of 58 Be stars that have been measured since 1998. The aim of the study is to understand the timescales of disk variability, formation and dissipation as a function of the properties (mass, luminosity and rotational velocity) of the underlying B star. In this paper we classified the sample based on the presence of emission or absorption of the H α line, and the shape of the peak as single or double peak, as well as noting changes between emission and non-emission states. We find a probability of ~ 0.75 percent per year that an object in the sample will undergo such a change. We also present re-derived values of the projected rotational velocities for the sample. When we compare our polarization values with those from the literature, we find that most of the stars do not show a change in the value of the polarization angle, however a small number show significant changes which could be attributed to either disk strength (optical depth) or geometry changes. Finally we show how, by combining the (interstellar corrected) degree of polarization and the projected rotational velocity, we can construct an inclination angle-free parameter that includes the true equatorial velocity. Using this inclination angle-independent parameter we show that the populations of single and double peak stars are indistinguishable, giving further evidence that Be star line profiles are essentially inclination angle driven.

Key words: techniques: spectroscopic – techniques: polarimetric – stars: emission-line, Be

1 INTRODUCTION

Be stars are, on a fundamental level, B stars that show, or have shown in the past, one or more Balmer lines in emission (Collins 1987). The origin of this emission is currently understood as a circumstellar disk around the star that has been created by material lost by the star (Poeckert & Marlborough 1978; Quirrenbach 1994).

The mechanism that creates this disk is still debated: It is understood that a rapid rotational velocity (v) plays an important role (Slettebak 1979), although in general they do not rotate at the full break-up velocities (Porter 1996). Mechanisms proposed include single-star radial pulsation (Baade 1988; Rivinius et al. 1998), but it is unclear if this is enough to create the disk (Owocki 2006; Cranmer 2009). Magnetic fields may also play a role (Cassinelli et al. 2002; Brown et al. 2008), but no magnetic fields have been found on Be stars, in contrast with B stars (Wade et al. 2014). Another possibility is that the creation of the disk is due to interaction with a companion star (Kriz & Harmanec 1975; Pols et al. 1991), where the accreting star in the transfer not only increases its mass but also its angular momentum (Hastings et al. 2021). A study from Oudmajer & Parr (2010) found that only $\sim 30\%$ of stars are found in binaries, while a study from Bodensteiner et al. (2020) found that while none of the Be stars studied were in visible binaries with main sequence stars, a large fraction of the fast-rotating B stars were, supporting the idea that binarity may be the cause of the fast rotation and the companion is barely visible anymore after the mass transfer. At the same time,

while no main sequence stars have been found as companions of Be systems, subdwarf O and B stars have been found, with characteristics similar to remnant core of a star that did lose most of its envelope (Mourard et al. 2015). A more detailed discussion on the importance of the binarity channel in the creation of the disk around the B star is given by Jones et al. (2022).

In order to help constrain models, observational studies of the properties and variability of the Be phenomenon are likely to be key. For example, understanding the timescales of disk loss and reformation as a property of stellar mass, temperature and equatorial velocity is likely to be important (Barnsley & Steele 2013). Understanding these dependencies is, however, complicated by the effect of inclination. The disk will have a certain inclination, i , with respect to the observation plane and the Earth. As a result, the observed rotational velocity is $v \sin i$. This value is useful as a lower bound for the rotational velocity, but at the same time the actual rotational velocity v can be much higher. An upper bound on the v will be the critical velocity (v_{crit}), at which point the rotational and gravitational forces at the equator of the star are balanced. A value often used to see how close to this point a star is the critical fraction $W = v/v_{\text{crit}}$.

The variability and shape of the emission line has also been a matter of study: It can be a single or double peak (Hanuschik et al. 1988) with variable values of asymmetry between the peaks (Hanuschik et al. 1995) or have the shape of shell lines (Hanuschik 1995). These profiles have been successfully modelled and theoretically reproduced (Silaj et al. 2010).

As well as showing emission line variability, the polarization of Be stars is also variable with time (Coyne & Gehrels 1967). The

* E-mail: a.castanonesteban@2019.ljmu.ac.uk

polarization is caused by radiation scattering due to free electrons (Coyne & Kruszewski 1969) and is a function of the inclination angle. As such the combination of spectroscopic and polarimetric observations can help constrain the true rotational velocity v .

In this paper we present the first in a series of new analyses of the properties of a sample of Be stars (Steele et al. 1999) that have been observed spectroscopically for more than two decades. The overall aim of the project is to understand the variability timescales of the objects and how that relates to the properties (mass, luminosity, rotational velocity) of the underlying B star. For this first paper we concentrate on combining new polarimetric observations with the historical spectral data in order to understand the rotational velocity distribution of the sample. This will then be used in future papers to explore the impact on line emission variability at various wavelengths.

In section 2 we describe the properties of the sample and previous work that has been carried out on it. In section 3 we describe the acquisition and data reduction of our spectroscopic and polarimetric dataset and in section 4 make a basic classification of the appearance and variability of the $H\alpha$ line profile for each object. Section 5 describes the calculation of projected rotational velocities and critical velocities for the sample. Similarly, section 6 describes the correction for each object of polarization degrees and angles for the effects of interstellar polarization. In Section 7 we combine the results of the previous two sections to derive rotational velocities corrected for the effect of inclination angle. Finally in section 8 we make some concluding remarks.

2 SAMPLE SELECTION

Our sample is the same as the one introduced in Steele et al. (1999). The 58 stars in the sample were initially classified as Be stars in the database presented in Jaschek & Egret (1982), and were selected to cover several objects for each spectral and luminosity class for Be stars, to make it as representative as possible. However, because Be stars are variable, some of the stars classified as Be stars in 1982 might not show $H\alpha$ emission anymore. As the raw data used in their initial classification is generally unavailable and was compiled from a wide variety of sources, they may also have been misclassified. Several of the stars might also have changed to no emission at some point before or between the observations.

Previous work on the sample is described in a series of five papers published between 1999 and 2013. In paper I (Steele et al. 1999), the criteria for the selection of the sample was presented. A basic study of the rotational velocities of the stars was done based on a single spectrum of each object, as well as a reclassification of their spectral type. Paper II (Clark & Steele 2000) studied the same sample plus another 8 sources in the K band (2.05–2.22 μ m). It determined that some objects do not show Bry emission ($\lambda = 21660 \text{ \AA}$), which might indicate no hydrogen emission in general, putting in doubt their classification as a Be star. Different sets of the spectra showed H I, He I, Mg II, Fe II and Na I lines, with He I and Mg II features as a good diagnostic of early spectral type. At the same time, stars that did not show Bry emission seemed to have a lower projected rotational velocity. Paper III (Steele & Clark 2001) studied 57 of the stars from paper I in the H band (1.53–1.69 μ m). H I Brackett lines were again examined, as well as Fe II. It showed that the analysis of the H band spectra alone only allows for the classification into "early" (B0e–B4e) and "late" (B5e–B9e) types. Paper IV (Howells et al. 2001) studied 52 of the stars from paper I with JHK infrared photometry, separating values for the interstellar reddening and the circumstellar excess, and

Table 1. The values given for the defocus of the telescope when using MOPTOP for the different sources, depending on their apparent magnitude V.

V	Defocus (mm)
$m > 9.75$	0.0
$9.75 > m > 6.75$	1.0
$6.75 > m > 4.9$	2.0
$4.9 > m > 4.04$	2.5

finding a strong correlation between the derived interstellar reddening values and the equivalent width of the interstellar sodium lines, giving confidence in the measured reddening. Paper V (Barnsley & Steele 2013) studied the equivalent width variability of the $H\alpha$ line for the measurements taken for 55 stars between 1998 and 2010, finding that stars of earlier types, with higher values of the projected rotational velocity, show a higher degree of variability in the $H\alpha$ emission.

3 DATA

3.1 Observations and Data Reduction

The objects in our sample have been observed several times between 1998 and 2022 with multiple instruments. This work includes observations taken in 1998 and 2002 using the IDS spectrograph on the Isaac Newton Telescope (INT), 2009 observations with the medium resolution settings ($R \sim 2500$) of the FRODOspec spectrograph on the Liverpool Telescope (LT) (Morales-Rueda et al. 2004), 2010 to 2021 observations with the high resolution ($R \sim 5000$) FRODOspec settings, and 2022 observations with the low resolution ($R \sim 350$) SPRAT spectrograph also on the LT (Piascik et al. 2014). The years of observation, as well as the total number of observations, are shown in Table A1. All INT and LT data were re-reduced using the ASPIRED pipeline (Lam et al. 2020) for consistency.

In addition to these spectra, we have polarimetric observations taken with the MOPTOP polarimeter on the Liverpool Telescope (Jermak et al. 2016, 2018) in October 2022. Our sample is very bright, with apparent magnitudes in the range of $V = 4.04$ and $V = 10.60$ (Steele et al. 1999). For this reason, if we try to observe the brightest objects directly, the observation will be instantly saturated. To avoid this, we defocussed the telescope, with different values depending on how bright the stars are, allowing us to spread the light without saturating the detector. We also used the MOPTOP fast-rotation mode, which completes a cycle of 16 positions in 8 seconds, to avoid saturation as much as possible. The values used for the defocussing are shown in Table 1 to aid future observers of bright objects with the instrument.

Reduction of the MOPTOP data was carried out using aperture photometry routines from ASTROPY (Astropy Collaboration et al. 2022). The extracted photometric counts were converted to Stokes q and u values following the procedure outlined in Shrestha et al. (2020), with corrections for instrumental polarization made using the calibration values presented in Steele et al. (2023).

3.2 Additional data

As additional data, we have included the distances and the reddening. The distances have been calculated from parallax values obtained from the Gaia database (Gaia Collaboration et al. 2022), except in 3 cases where they have been taken from the Hipparcos catalog (van Leeuwen 2007) because they were not available or the error of the

Gaia values was larger than the actual values. The reddening $E(B-V)$ was obtained in [Howells et al. \(2001\)](#), where we could find values for 52 of the stars in our data. These values have been added to Table [A2](#).

4 H α CLASSIFICATION

The most basic classification that we can make for Be stars from their spectra is taking into account the shape of the H α line: some Be stars will show a single peak emission, while others will show a mostly symmetric double peak emission. We show an example of this in Figure 1. At the same time, others will not show any H α emission anymore, and will show absorption of the line instead. Even more interesting, with a long time study like this one, we can also see some changing with time. We will discuss this in a quantitative fashion in future papers. However for now we simply classify them based on their overall appearance. In the most complicated cases of the ones with changing emission type, we will choose the most recent observation, as it is the most closely related to their polarization status.

From our sample of 58 stars, 10 never showed any H α emission between 1998 and our last observation. 16 show a single peak in all of our observations, while 21 show a double peak in all of them. The remaining 11 in our sample have changed with time, with 3 of them showing emission and 8 not showing emission in our last observation. In total, from our last observation, 18 do not show hydrogen emission and 40 show hydrogen emission lines (Figure 2).

Examining the 11 objects that changed with time in more detail, we see that 9 of them at least spent some time as no emission, with another 2 always emitting and changing only between double peak and single peak. We can therefore assume a change rate between emission and absorption of 9/48 in 24 years, or 0.78% of the total sample changing between emission and absorption every year (counting only the objects that we have observed actively changing from our first observation). Similarly if we instead assume all the objects that did not show any absorption in 1998 are changed from their original observations, compiled in [Jaschek & Egret \(1982\)](#) but originally from the 1960s and 1970s, we would have a fraction 19/58 over an estimated time of 45 years (0.73%/year).

Previous determinations of this change rate ([McSwain et al. 2008, 2009; Barnsley & Steele 2013; Dimitrov et al. 2018](#)) over shorter time periods (4–12 years) have ranged between 0.3 and 25 %/year. This wide range can be attributed to how the different samples used for the studies were constructed. Using the same sample as here but only between 1998 and 2010 [Barnsley & Steele \(2013\)](#) found 2 changing objects over 55 analyzed Be stars over a period of 12 years, or 0.30%/year. However ([McSwain et al. 2008](#)) observed 16 Be stars in a sample of 191 B stars, with 11 of them changing between emission and no emission during a period of observation of 4 years. If these 11 are counted only from the 16 Be stars, then the change rate would be of 11/16 over 4 years, or 17%/year. Alternatively if we count them over the whole sample of B stars, then the change rate would be 11/191 over 4 years, or 1.4%/year. A similar study [McSwain et al. \(2009\)](#) observed 45 Be stars in a sample of 296 B stars over 2 years, with 23 of them showing variability in emission. Counting only 23/45 for 2 years would give us a change rate of 25.5%/year, while 23/296 for 2 years would give us instead a change rate of 3.89%/year. Finally [Dimitrov et al. \(2018\)](#) observed 60 Be stars over a period on 3 years, and 4 of them changed in emission giving a change rate of 2.2%/year. Overall comparing the values with at least similar methodologies (including our latest determination) it

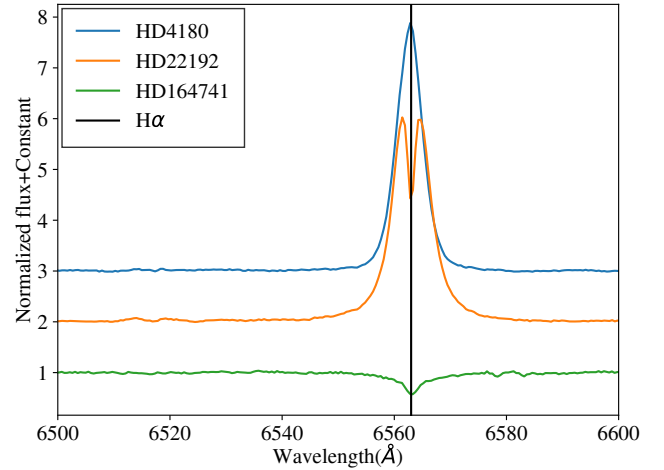


Figure 1. Representative plots of the three types of H α peaks in our sample, extracted from the 1998 observations. HD4180 is an example of a single peak, HD22192 is an example of a double peak, and HD164741 is instead an example of absorption in H α . The rest wavelength of H α is indicated by the vertical line.

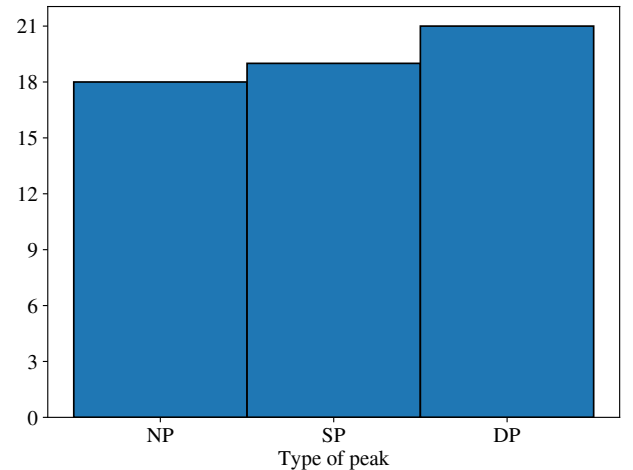


Figure 2. The distribution of our sample for the three different types of observed H α , in this case, "NP" for "No peak", "SP" for "Single peak", and "DP" for "Double peak", classified from their last observation.

appears that a change rate of no more than a few percent per year is something like the true value.

5 RESULTS: ROTATION

5.1 Calculation of the rotational velocities

One of the most common values for Be stars is the rotational velocity of the central star, $v\sin i$. The way that we have chosen to obtain these values is using the He-I absorption lines in our spectra, more precisely the lines at wavelengths 4026 Å, 4143 Å, 4387 Å and 4471 Å. We first fit a Gaussian profile to each of these lines, obtaining this way σ , the standard deviation of the Gaussian distribution, that then

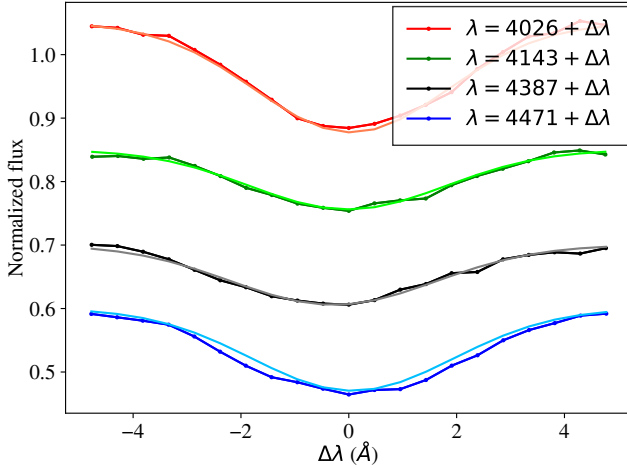


Figure 3. A plot, showing the fit to the helium I lines. In this case, it is the observation of star HD4180 taken in August 1998. We fit each line to a Gaussian profile and obtained the FWHM from them, and hence the velocity as described in Section 5. The results for each line in this example are $v\sin i(\lambda = 4026\text{Å}) = 193.7 \pm 3.2 \text{ km/s}$, $v\sin i(\lambda = 4143\text{Å}) = 190.8 \pm 4.9 \text{ km/s}$, $v\sin i(\lambda = 4387\text{Å}) = 187.7 \pm 4.9 \text{ km/s}$, $v\sin i(\lambda = 4471\text{Å}) = 181.9 \pm 3.9 \text{ km/s}$.

can be converted into the full width half maximum (FWHM) using:

$$FWHM = 2\sqrt{2 \ln 2}\sigma \quad (1)$$

These values of FWHM are not yet a measurement of the rotational velocity itself, since rotation is not the only line broadening mechanism. We therefore convert them using the $FWHM-v\sin i$ relation derived from observational fits to rotationally broadened line profiles of model atmospheres of a wide sample of early type stars (Slettebak et al. 1975). We will first do a linear fit for the values of FWHM and $v\sin i$ of the He-I line ($\lambda = 4471\text{Å}$) shown in the tables 1 and 2 of Slettebak et al. (1975), as shown in Figure 4, and then use this relation to convert our values to rotational velocities, applying a Doppler shift to the FWHM dependent slope to change the values to the other three near He-I lines ($\lambda = 4387\text{ Å}, \lambda = 4143\text{ Å}, \lambda = 4026\text{ Å}$). The final equations obtained were:

$$\begin{aligned} v\sin i &= 42.68F(\lambda = 4471) - 36.84\text{km s}^{-1} \\ v\sin i &= 43.50F(\lambda = 4387) - 36.84\text{km s}^{-1} \\ v\sin i &= 46.06F(\lambda = 4143) - 36.84\text{km s}^{-1} \\ v\sin i &= 47.40F(\lambda = 4026) - 36.84\text{km s}^{-1} \end{aligned} \quad (2)$$

with $F(\lambda)$ being the FWHM for the line at the corresponding wavelength.

For any particular object the results of the fits to these lines will show certain variation: a number of factors can cause this effect such as the noise in the spectrum or blending with another line. For that reason, we have chosen to calculate the weighted mean and standard deviation of the four lines and reject any values that are more than 4 σ away from the average value. With this, we have obtained a series of values in time for the rotational velocity of the star. We do not expect any changes in the rotational velocity of a star over the span of just a few decades, so we take the weighted mean of these values for each object. These results are shown in Table 2 and represented in Figure 5.

Table 2. List of observed objects, comparing their rotational velocities vs the rotational velocities obtained in Steele et al. (1999)

Object	Other Identifier	$v\sin i$ (km/s) (2023)	$v\sin i$ (km/s) (1999)
CD-28 14778	HD 171757	141 ± 23	153 ± 21
CD-27 11872	HD 161103	210 ± 17	224 ± 33
CD-27 16010	HD 214748	188.6 ± 7.2	187 ± 32
CD-25 12642	HD 164741	100 ± 24	77 ± 18
CD-22 13183	HD 172158	169 ± 79	174 ± 10
BD-20 5381	HD 177015	197 ± 72	202 ± 10
BD-19 5036	HD 170682	126 ± 17	121 ± 10
BD-12 5132	HD 172252	98 ± 11	120 ± 43
BD-02 5328	HD 196712	170.2 ± 8.4	151 ± 15
BD-01 3834	HD 187350	166 ± 12	168 ± 34
BD-00 3543	HD 173371	224 ± 15	271 ± 54
BD+02 3815	HD 179343	197 ± 10	224 ± 14
BD+05 3704	HD 168797	211 ± 59	221 ± 10
BD+17 4087	HD 350559	204 ± 79	156 ± 39
BD+19 578	HD 23016	215 ± 17	240 ± 70
BD+20 4449	HD 191531	90 ± 43	81 ± 11
BD+21 4695	HD 210129	157 ± 17	146 ± 10
BD+23 1148	HD 250289	87 ± 77	101 ± 10
BD+25 4083	HD 339483	161 ± 83	79 ± 11
BD+27 797	HD 244894	197 ± 18	148 ± 74
BD+27 850	HD 246878	121 ± 18	112 ± 25
BD+27 3411	HD 183914	170 ± 13	194 ± 10
BD+28 3598	HD 333452	113 ± 50	90 ± 12
BD+29 3842	HD 333226	81 ± 20	91 ± 16
BD+29 4453	HD 205618	247 ± 26	317 ± 20
BD+30 3227	HD 171406	207.5 ± 8.3	218 ± 21
BD+31 4018	HD 193009	225 ± 30	211 ± 11
BD+36 3946	HD 228438	178 ± 23	186 ± 21
BD+37 675	HD 18552	223 ± 21	207 ± 29
BD+37 3856	HD 228650	119 ± 18	104 ± 17
BD+40 1213	HD 33604	122.3 ± 7.4	128 ± 20
BD+42 1376	HD 37657	195.6 ± 9.6	196 ± 10
BD+42 4538	HD 216581	236 ± 30	282 ± 10
BD+43 1048	HD 276738	205 ± 46	220 ± 20
BD+45 933	HD 27846	135 ± 14	148 ± 16
BD+45 3879	HD 211835	186 ± 10	193 ± 10
BD+46 275	HD 6811	111 ± 20	113 ± 21
BD+47 183	HD 4180	167 ± 12	173 ± 12
BD+47 857	HD 22192	227 ± 12	212 ± 16
BD+47 939	HD 25940	153.0 ± 8.0	163 ± 12
BD+47 3985	HD 217050	232 ± 14	284 ± 20
BD+49 614	HD 13867	140 ± 110	90 ± 27
BD+50 825	HD 23552	184 ± 11	187 ± 10
BD+50 3430	HD 207232	198 ± 19	230 ± 15
BD+51 3091	HD 20551	139.8 ± 8.5	106 ± 10
BD+53 2599	HD 203356	223 ± 22	191 ± 23
BD+55 552	HD 13669	243 ± 29	292 ± 17
BD+55 605	HD 14605	142 ± 25	126 ± 35
BD+55 2411	HD 195554	192.8 ± 9.2	159 ± 90
BD+56 473	V356 Per	218 ± 23	238 ± 19
BD+56 478	HD 13890	152 ± 30	157 ± 12
BD+56 484	V502 Per	182 ± 39	173 ± 16
BD+56 493	-	175 ± 41	270 ± 10
BD+56 511	-	108 ± 54	99 ± 14
BD+56 573	-	210 ± 51	250 ± 58
BD+57 681	HD 237056	155 ± 20	147 ± 49
BD+58 554	HD 237060	209 ± 17	229 ± 10
BD+58 2320	HD 239758	244 ± 39	243 ± 20

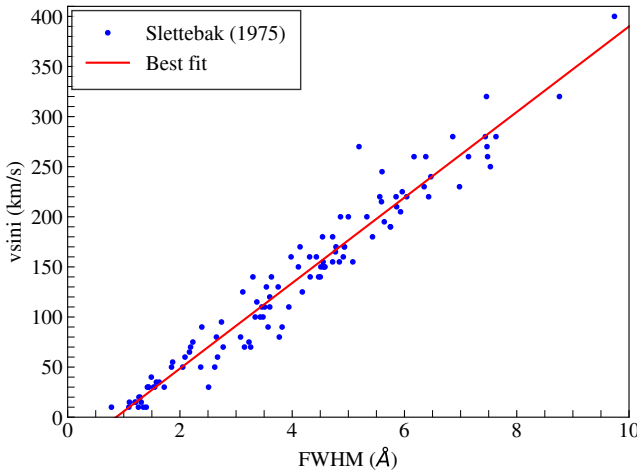


Figure 4. A plot of the rotational velocities of B stars vs the FWHM of the He I 4471 Åline, extracted from tables 1 and 2 in Slettebak et al. (1975). The results of the linear fit $y = Ax + B$ are $A = 42.68 \pm 0.93$, $B = -36.84 \pm 4.17$, $R = 0.9746$

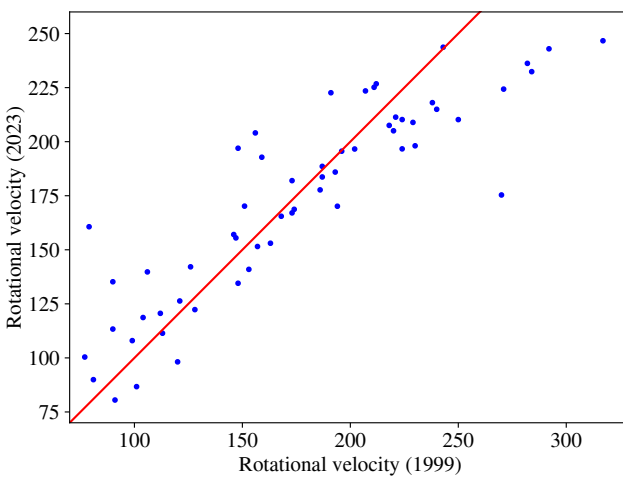


Figure 5. A plot comparing the values obtained for the rotational velocity in 2023 vs the values obtained for the rotational velocity in 1999. The red line is a 1:1 line for comparison that allows us to see that our rotational velocities seem to be similar when compared with the lower values of 1999, but lower when compared with the higher values of 1999. The cause of this difference might be that our results are the average of many years of observations, versus only one observation as in 1999.

5.2 Calculation of the critical velocity

The critical velocity of a Be star is the theoretical equilibrium velocity at which the central B star would need to rotate over to eject the material on its equator purely by compensating gravity with rotation. We can find the formula for example in Townsend et al. (2004):

$$v_{crit} = \sqrt{\frac{2}{3} \frac{GM}{R_P}} \quad (3)$$

with M the mass of the central star and R_P its polar radius.

To obtain these values for our sample, we use classification of the spectral types from Steele et al. (1999) (reproduced in our Table

A2) to take stellar luminosities from de Jager & Nieuwenhuijzen (1987); Cox (2000). Masses and radii were then derived from those luminosity values using the equations shown in Tables 4 and 5 of Eker et al. (2018).

First, we have calculated the masses from the luminosities, following the set of equations:

$$\begin{aligned} \log M &= (\log L - 0.010)/4.329; 1.05 < M/M_\odot \leq 2.40 \\ \log M &= (\log L - 0.093)/3.967; 2.4 < M/M_\odot \leq 7 \\ \log M &= (\log L - 1.105)/2.865; 7 < M/M_\odot \end{aligned} \quad (4)$$

calculating the three values and choosing the appropriate ones for their range.

From those values, and following the indications in Eker et al. (2018), we have calculated as well the effective temperature:

$$\log T_{\text{eff}} = -0.170(\log M)^2 + 0.888 \log M + 3.671 \quad (5)$$

and then we finally calculate the radius of the star using Stefan-Boltzmann law:

$$R = \sqrt{\frac{L}{4\pi\sigma T_{\text{eff}}^4}} \quad (6)$$

After obtaining the values of the mass and radius of the star, we can calculate the v_{crit} and the value of the critical fraction W , to show how close the obtained equatorial rotational velocity is to the critical value:

$$W = \frac{v}{v_{crit}} \quad (7)$$

We have also calculated the value of $W v_{sin i}$, where in equation 7 we used $v_{sin i}$ instead of v . All of these values are listed in Table A2.

6 RESULTS: POLARIZATION

6.1 Calculation of the polarization degree and angle

After calculating the values for the rotational velocity ($v \sin i$), we move to the calculation of the polarization degree and angle of each band. We first calculate the Stokes parameters following the instructions for the double camera settings as shown in Shrestha et al. (2020). After obtaining the Stokes parameters, we calculated the polarization degree and angle for each band according to the standard formulation. We have derived the polarization degree (P) and angle (θ) values for the bands V , B and R . These results can be found in Tables A3 and A4. As most of the values that we will compare our polarization values (section 7) with are full-range/white-light instead of individual bands, we have calculated the average of the values q and u for the three bands and calculated the average values for the polarization degree (\bar{P}) and the angle ($\bar{\theta}$) from them.

We note here that MOPTOP polarimetry suffers from a systematic errors of ~ 0.002 in P and 1° in θ (Shrestha et al. 2020). These systematic errors are not included in the values presented in Tables A3 and A4 but are incorporated into the final interstellar corrected values calculated in the next section.

6.2 Separation of the interstellar and intrinsic polarization

We have attempted to separate interstellar polarization from the total polarization. To obtain the values for the interstellar polarization we have first selected stars from the 9286 object catalogue (Heiles 2000) within an angular distance of 5 degrees on the sky from each

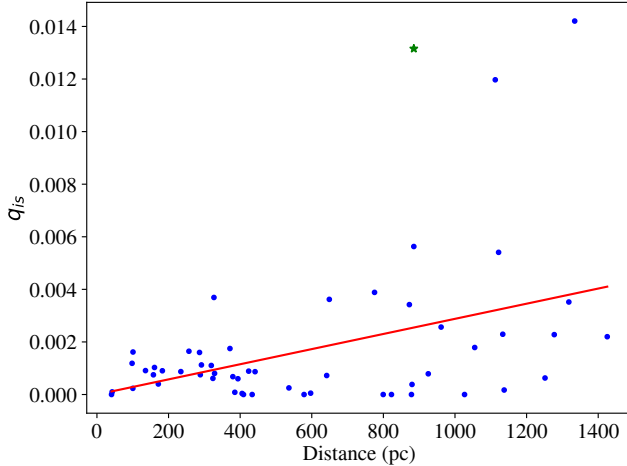


Figure 6. Here we see the polarization coefficient q of nearby stars (in blue) compared to our object, BD+31 4018 (in green). The red line is a fit to the nearby star data.

of our sample stars. We then found the distances to these group of stars using the Gaia catalog. We have separated the values of the Stokes parameters q and u from the catalogue polarization degree and angle for these stars, then performed a linear fit to them to find the values of interstellar q and u with respect the distance. Then we calculated q_{is} and u_{is} for our sample stars depending on their distance, using the previous linear fit, as shown in Figure 6. The errors for the interstellar polarization are derived from the values of the linear fit. We then subtracted the values of the interstellar q and u for our sample stars from the total values of their Stokes parameters, obtaining the intrinsic values (q_{in} and u_{in}), and then calculated the values for both the interstellar and intrinsic polarization degree and angle as shown in Table A7.

7 ANALYSIS

7.1 Comparison of \bar{P} and $\bar{\theta}$ with other authors

41 of the stars in our sample have had polarization measurements previously, so we can compare our values for \bar{P} and $\bar{\theta}$ to the ones from previous authors. The sources for these reference values are Hall (1958), Behr (1959), Coyne & Gehrels (1967), Coyne & Kruszewski (1969), Serkowski (1968), Serkowski (1970), McLean & Clarke (1976), Coyne (1976), Poeckert & Marlborough (1976), McLean & Brown (1978) and Yudin (2001). We have reduced these to 1950s, 1960s, 1970s and 2000s for simplicity, taking the average of all values where there is more than one.

In Table 3 we compare our values with the most studied Be stars from our sample, for a historical perspective, while in Table A5 we compare our entire sample with the ones from Yudin (2001). We can see that the polarization degree changes with time, and while the polarization angle is mostly constant (Figure 7), there are a number of objects with significant ($> 10^\circ$) changes over the 70 year time baseline. We highlight these objects in bold in Table 3. We note that large changes in polarization angle are typically associated with large changes in the degree of polarization (either positive or negative). However, we note that the objects that show such angle changes seem to be spread fairly evenly between those which do and do not show changes in the H α peak morphology (see last line of table).

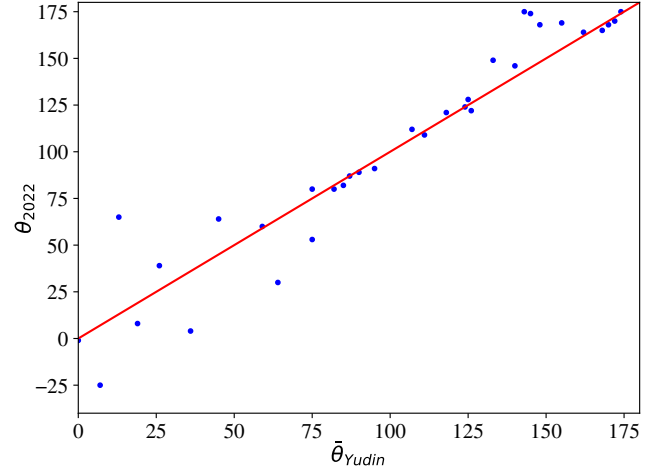


Figure 7. A plot of our (2022) polarization angles vs the polarization angles measured by Yudin (2001).

Overall the changing polarization angle can be interpreted as either a varying ratio of interstellar and circumstellar polarization (which naturally have random polarization angles with respect to each other) as the disk strength varies, or as a change in the disk geometry as a function of time. Such behaviour has, for example, been seen in the interferometric and polarimetric measurements presented by Quirrenbach et al. (1997). We will explore this question on an object-by-object basis in a future paper.

7.2 Removal of the inclination dependence

As radiation escapes the Be star and is scattered through the disk, it will get polarized. This polarization has been modeled by Brown & McLean (1977):

$$P \simeq \bar{\tau}(1 - 3\gamma) \sin^2 i \quad (8)$$

with P the polarization degree, $\bar{\tau}$ the average electron optical depth, γ a shape factor that describes the asymmetry of the disk, and i the inclination.

It is impossible for us to separate these values without knowing the value of the inclination. However, as we have measured previously the rotational velocity $v \sin i$, this allows us to obtain instead:

$$\frac{P}{(v \sin i)^2} = \frac{K}{v^2} \quad (9)$$

with $K = \bar{\tau}(1 - 3\gamma)$.

This allows us to derive a value for v that is not dependent on the inclination of the star (although there is now an uncertainty related to the mean optical depth instead). Similarly we can multiply the values shown in equation 9 by the critical velocity:

$$\frac{P}{(v \sin i)^2} v_{\text{crit}}^2 = \frac{K}{v^2} v_{\text{crit}}^2 = \frac{K}{W^2} \quad (10)$$

obtaining a measurement of the critical fraction W .

7.3 Testing the population differences

In order to test the validity of the above procedure, we can compare the distribution of the various quantities $v \sin i$, $W \sin i$, W^2/K and v^2/K

Table 3. The values \bar{P} and $\bar{\theta}$ shown here are the weighted average of their years. For the 1950s, we have used the ones shown in Hall (1958) and Behr (1959), for the 1960s we have used the ones shown in Coyne & Gehrels (1967), Coyne & Kruszewski (1969) and Serkowski (1968), for the 1970 we have used Serkowski (1970), McLean & Clarke (1976), Coyne (1976), Poeckert & Marlborough (1976) and McLean & Brown (1978), for 2001 we have used the ones shown in Yudin (2001), and for 2022 our own calculated values. In bold, the values for the polarization angles that have shown a difference bigger than 10° over the past 70 years.

Object	Other identifier	1950s		1960s		1970s		2001		2022		Peak
		\bar{P} (%)	$\bar{\theta}$									
CD-27 11872	HD 161103	11.1	171	-	-	-	-	4.83	172	7.1	170	SP
CD-27 16010	HD 214748	-	-	-	-	1.75	163	0.09	155	0.4	169	DP
CD-25 12642	HD 164741	1.7	14	-	-	-	-	-	-	3.2	14	NP
CD-22 13183	HD 172158	1.7	178	-	-	-	-	4.65	143	1.2	175	SP
BD-20 5381	HD 177015	1.1	0	-	-	-	-	0.51	0	1.3	179	DP
BD-01 3834	HD 187350	1.7	82	-	-	-	-	0.78	82	0.4	80	SP
BD+05 3704	HD 168797	1.7	64	-	-	-	-	0.78	64	1.4	30	Change
BD+19 578	HD 23016	-	-	-	-	1.48	87	0.60	87	0.5	87	Change
BD+29 4453	HD 205618	2.7	26	-	-	-	-	1.24	26	1.0	39	SP
BD+30 3227	HD 171406	0.6	13	-	-	-	-	0.28	13	1.6	65	Change
BD+31 4018	HD 193009	1.4	75	-	-	-	-	0.65	75	1.4	80	SP
BD+40 1213	HD 33604	2.8	168	-	-	-	-	1.29	168	1.5	165	SP
BD+42 1376	HD 37657	3.6	174	-	-	-	-	1.66	174	1.5	175	Change
BD+46 275	HD 6811	2.08	90	-	-	8.75	94	7.4	90	0.9	89	Change
BD+47 183	HD 4180	1.975	84	1.05	84	0.815	82	0.70	85	1.1	82	SP
BD+47 857	HD 22192	1.55	42	-	-	1.07	42	0.80	45	0.2	64	DP
BD+47 939	HD 25940	2.28	173	1.09	158	1.025	172	0.25	145	1.1	174	SP
BD+47 3985	HD 217050	3.9	75	1.65	69	1.123	71	1.55	75	0.4	53	Change
BD+55 605	HD 14605	8.2	118	-	-	-	-	3.78	118	4.2	121	Change
BD+56 478	HD 13890	7.5	107	-	-	-	-	3.46	107	3.7	112	DP

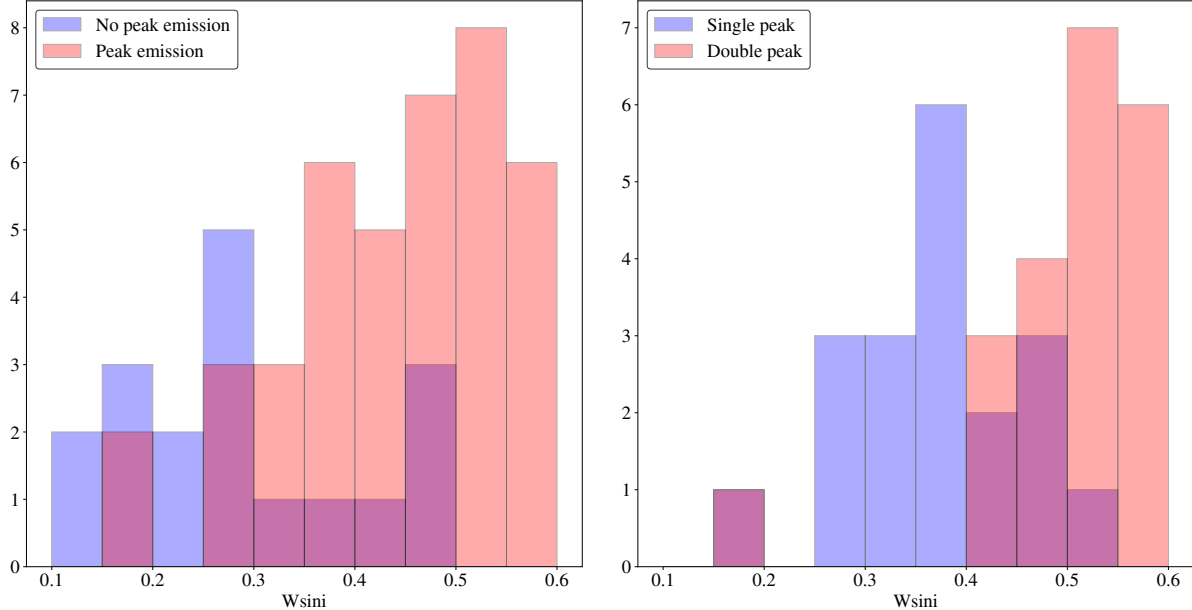


Figure 8. Two histograms showing the distribution of stars for different values and types of emission of the $H\alpha$ line with respect to $W\sin i$.

against the $H\alpha$ emission classification we made in Section 4. To do this we used Kolmogorov-Smirnov tests to compare the histograms of these quantities for the permutations of no- (NP), single peaked- (SP), and double peaked-emission DP). The results of the tests are shown in Table 4.

In all cases, when considering the distributions that include the $\sin i$ inclination term, the distributions for different $H\alpha$ emission properties all indicate a different parent population.

For example Figure 8 (left) shows the distributions of P and NP objects are different in terms of $W \sin i$, with the first showing showing faster $W \sin i$ associated with $H\alpha$ emission, and the showing slower $W \sin i$ associated with $H\alpha$ absorption as expected from previous studies.

Similarly the right panel shows the difference between single and double peaks, with double peaks seemingly rotating faster in terms of $W \sin i$. However, when we remove the angular dependence on

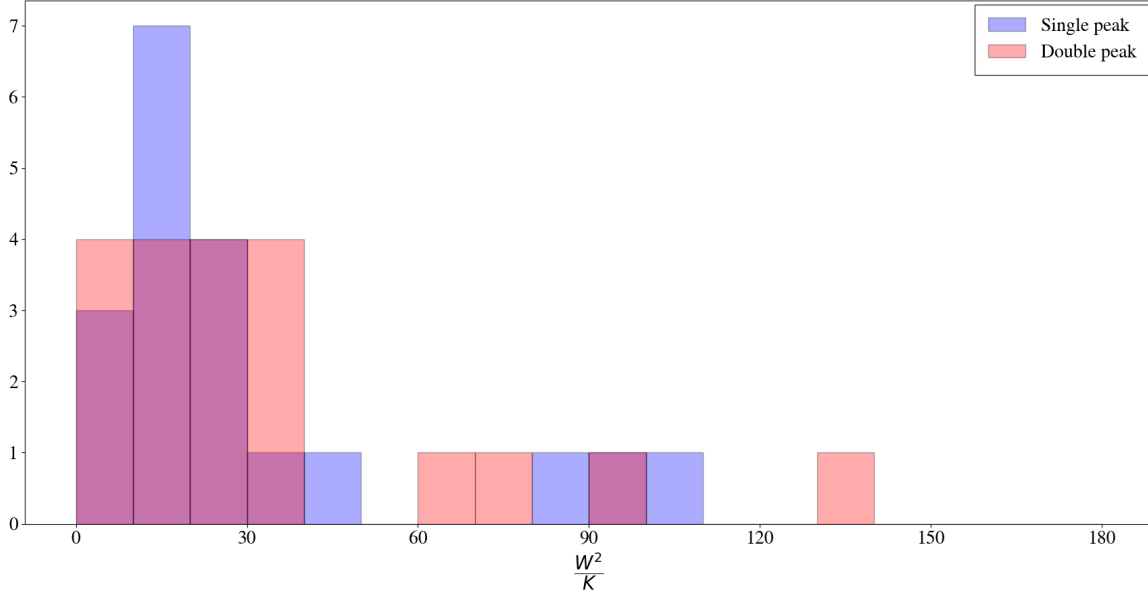


Figure 9. A histogram showing the distribution of stars for single and double peak $H\alpha$ line with respect to $\frac{W^2}{K}$.

Table 4. Results from the KS tests. Distributions which are apparently drawn from the same parent population (i.e. $p > 0.05$) are highlighted in bold.

Values	NP vs P	NP vs SP	NP vs DP	SP vs DP
$v \sin i$	0.00	0.04	0.00	0.00
$W \sin i$	0.00	0.01	0.00	0.00
W^2/K	-	-	-	0.64
v^2/K	-	-	-	0.98

the inclination (W^2/K) the null hypothesis can not be rejected [9](#). This can be interpreted as evidence for the idea that the cause of the difference between single and double peak $H\alpha$ emission is the inclination of the disk, as predicted by emission line modelling (e.g. [Poeckert & Marlborough \(1976, 1978\)](#), [Sigut et al. \(2020\)](#)). If that theory is taken as accepted, then our method of using polarization to eliminate the dependence on the inclination angle appears to work for the sample distribution.

8 CONCLUSIONS

Using a sample of 58 stars previously classified as Be, we have used spectra taken over multiple epochs over a 24 year period to classify them based on their qualitative $H\alpha$ line appearance. We classified these stars in three groups depending on whether they have emission in the shape of a single peak, in the shape of a double peak, or no emission. We found a probability of ~ 0.75 percent per year that an object would change state between emission and non-emission.

We also calculated the projected rotational velocity ($v \sin i$) from multiple measurements of the He-I line profiles. We then compared polarization measurements taken in 2022 with those from previous authors, revealing that the majority of objects show no significant changes in the polarization angle. This is to be expected if this were a mainly geometric parameter based on the system having a stable

3d space orientation. However we do find a small sample of objects which seem to show genuine polarization angle variability which may be interpreted as either varying disk strength (optical depth) or geometry. This will be investigated further in a future paper.

For each object we have used the degree of polarization to estimate a quantity that, when combined with the $v \sin i$, is related to the true equatorial rotational velocities. We find a clear separation between Be stars with $H\alpha$ emission and stars that do not emit. Once the angular inclination factor is removed, the populations of single and double peak $H\alpha$ emitters are indistinguishable at least on a population basis. In a future paper we will consider how to use quantitative measures of the variability of emission line properties of the objects in conjunction with this approach to constrain variability timescales in an inclination-independent fashion.

ACKNOWLEDGEMENTS

We want to thank the Isaac Newton Group of Telescopes and the Liverpool Telescope for providing the measurements used for this publication. This paper makes use of data obtained from the Isaac Newton Group of Telescopes Archive which is maintained as part of the CASU Astronomical Data Centre at the Institute of Astronomy, Cambridge. The Liverpool Telescope is operated on the island of La Palma by Liverpool John Moores University in the Spanish Observatorio del Roque de los Muchachos of the Instituto de Astrofísica de Canarias with financial support from the UK Science and Technology Facilities Council under UKRI grant ST/T00147X/1. The authors want to thank Maurizio Salaris for his help with some of the calculations. ACE thanks LJMU for financial support for his PhD studentship.

DATA AVAILABILITY

All the data used for this publication is publicly available on the Isaac Newton Telescope and Liverpool Telescope data archives.

REFERENCES

- Astropy Collaboration et al., 2022, [ApJ, 935, 167](#)
- Baade D., 1988, in Cayrel de Strobel G., Spite M., eds, The Impact of Very High S/N Spectroscopy on Stellar Physics. International Astronomical Union, Symposium no. 132, p. 217
- Barnsley R. M., Steele I. A., 2013, [A&A, 556, A81](#)
- Behr A., 1959, Veroeffentlichungen der Universitaets-Sternwarte zu Goettingen, [7, 199](#)
- Bodensteiner J., Shenar T., Sana H., 2020, [A&A, 641, A42](#)
- Brown J. C., McLean I. S., 1977, [A&A, 57, 141](#)
- Brown J. C., Cassinelli J. P., Maheswaran M., 2008, [ApJ, 688, 1320](#)
- Cassinelli J. P., Brown J. C., Maheswaran M., Miller N. A., Telfer D. C., 2002, [ApJ, 578, 951](#)
- Clark J. S., Steele I. A., 2000, [A&AS, 141, 65](#)
- Collins George W. I., 1987, in Slettebak A., Snow T. P., eds, IAU Colloq. 92: Physics of Be Stars. p. 3
- Cox A. N., 2000, Allen's Astrophysical Quantities
- Coyne G. V., 1976, [A&A, 49, 89](#)
- Coyne G. V., Gehrels T., 1967, [AJ, 72, 887](#)
- Coyne G. V., Kruszewski A., 1969, [AJ, 74, 528](#)
- Cranmer S. R., 2009, [ApJ, 701, 396](#)
- Dimitrov D. P., Kjurkchieva D. P., Ivanov E. I., 2018, [AJ, 156, 61](#)
- Eker Z., et al., 2018, [MNRAS, 479, 5491](#)
- Gaia Collaboration et al., 2022, [arXiv e-prints](#), p. arXiv:2208.00211
- Hall J. S., 1958, Publications of the U.S. Naval Observatory Second Series, [17, 275](#)
- Hanuschik R. W., 1995, [A&A, 295, 423](#)
- Hanuschik R. W., Kozok J. R., Kaiser D., 1988, [A&A, 189, 147](#)
- Hanuschik R. W., Hummel W., Dietle O., Sutorius E., 1995, [A&A, 300, 163](#)
- Hastings B., Langer N., Wang C., Schootemeijer A., Milone A. P., 2021, [A&A, 653, A144](#)
- Heiles C., 2000, [AJ, 119, 923](#)
- Howells L., Steele I. A., Porter J. M., Etherton J., 2001, [A&A, 369, 99](#)
- Jaschek M., Egret D., 1982, Proc. IAU Symp., [98, 261](#)
- Jermak H., Steele I. A., Smith R. J., 2016, in Evans C. J., Simard L., Takami H., eds, Society of Photo-Optical Instrumentation Engineers (SPIE) Conference Series Vol. 9908, Ground-based and Airborne Instrumentation for Astronomy VI. p. 99084I, doi:10.1111/12.2232324
- Jermak H., Steele I. A., Smith R. J., 2018, in Evans C. J., Simard L., Takami H., eds, Society of Photo-Optical Instrumentation Engineers (SPIE) Conference Series Vol. 10702, Ground-based and Airborne Instrumentation for Astronomy VII. p. 107024Q, doi:10.1111/12.2312132
- Jones C. E., et al., 2022, [Ap&SS, 367, 124](#)
- Kriz S., Harmanec P., 1975, Bulletin of the Astronomical Institutes of Czechoslovakia, [26, 65](#)
- Lam M. C., Smith R. J., Veitch-Michaelis J., Steele I. A., McWhirter P. R., 2020, [arXiv e-prints](#), p. arXiv:2012.03505
- McLean I. S., Brown J. C., 1978, [A&A, 69, 291](#)
- McLean I. S., Clarke D., 1976, in Slettebak A., ed., IAU Symposium Vol. 70, Be and Shell Stars. p. 261
- McSwain M. V., Huang W., Gies D. R., Grundstrom E. D., Townsend R. H. D., 2008, [ApJ, 672, 590](#)
- McSwain M. V., Huang W., Gies D. R., 2009, [ApJ, 700, 1216](#)
- Morales-Rueda L., Carter D., Steele I. A., Charles P. A., Worswick S., 2004, [Astronomische Nachrichten, 325, 215](#)
- Mourard D., et al., 2015, [A&A, 577, A51](#)
- Oudmaijer R. D., Parr A. M., 2010, [MNRAS, 405, 2439](#)
- Owocki S., 2006, in Kraus M., Miroshnichenko A. S., eds, Astronomical Society of the Pacific Conference Series Vol. 355, Stars with the B[e] Phenomenon. p. 219
- Piasek A. S., Steele I. A., Bates S. D., Mottram C. J., Smith R. J., Barnsley R. M., Bolton B., 2014, in Ramsay S. K., McLean I. S., Takami H., eds, Society of Photo-Optical Instrumentation Engineers (SPIE) Conference Series Vol. 9147, Ground-based and Airborne Instrumentation for Astronomy V. p. 91478H, doi:10.1111/12.2055117
- Poeckert R., Marlborough J. M., 1976, [ApJ, 206, 182](#)
- Poeckert R., Marlborough J. M., 1978, [ApJ, 220, 940](#)
- Pols O. R., Cote J., Waters L. B. F. M., Heise J., 1991, [A&A, 241, 419](#)
- Porter J. M., 1996, [MNRAS, 280, L31](#)
- Quirrenbach A., 1994, in Balona L. A., Henrichs H. F., Le Contel J. M., eds, Pulsation; Rotation; and Mass Loss in Early-Type Stars. Astronomical Union, Symposium 162, p. 450
- Quirrenbach A., et al., 1997, [ApJ, 479, 477](#)
- Rivinius T., Baade D., Stefl S., et al. 1998, in Kaper L., Fullerton A. W., eds, Cyclical Variability in Stellar Winds. ESO Astrophysics Symposia. p. 207
- Serkowski K., 1968, [ApJ, 154, 115](#)
- Serkowski K., 1970, [ApJ, 160, 1083](#)
- Shrestha M., Steele I. A., Piasek A. S., Jermak H., Smith R. J., Copperwheat C. M., 2020, [MNRAS, 494, 4676](#)
- Sigut T. A. A., Mahjour A. K., Tycner C., 2020, [ApJ, 894, 18](#)
- Silaj J., Jones C. E., Tycner C., Sigut T. A. A., Smith A. D., 2010, [ApJS, 187, 228](#)
- Slettebak A., 1979, [Space Sci. Rev. 23, 541](#)
- Slettebak A., Collins G., Boyce P., White N. M., Parkinson T., 1975, Astrophysical Journal Supplement Series (Supplement no. 281), vol. 29, May 1975, p. 137-159. Research supported by the Ohio State University, 29, 137
- Steele I. A., Clark J. S., 2001, [A&A, 371, 643](#)
- Steele I. A., Negueruela I., Clark J. S., 1999, [A&AS, 137, 147](#)
- Steele I. A., Wiersema K., McCall C., Newsam A., Shrestha M., 2023, [MNRAS, 518, 1214](#)
- Townsend R. H. D., Owocki S. P., Howarth I. D., 2004, [MNRAS, 350, 189](#)
- Wade G. A., Petit V., Grunhut J., Neiner C., 2014, [arXiv e-prints](#), p. arXiv:1411.6165
- Yudin R. V., 2001, [A&A, 368, 912](#)
- de Jager C., Nieuwenhuijzen H., 1987, [A&A, 177, 217](#)
- van Leeuwen F., 2007, [A&A, 474, 653](#)

APPENDIX A: TABLES OF DATA

We have added here some tables that were too big to be inserted in the paper.

This paper has been typeset from a \TeX / \LaTeX file prepared by the author.

Table A1. The list of observations taken for the respective objects.

Object	Alias	Observation dates	Total number of observations
CD-28 14778	HD 171757	1998, 2010, 2018, 2019	6
CD-27 11872	V3892 Sgr, HD 161103	1998, 2009, 2010, 2018, 2019, 2020	9
CD-27 16010	ϵ PsA, HR 8628, HD 214748	1998, 2009, 2010, 2013, 2018, 2019, 2020, 2022	15
CD-25 12642	HD 164741	1998, 2009, 2010, 2018, 2019, 2020	8
CD-22 13183	HD 172158	1998, 2009, 2010	3
BD-20 5381	HD 177015	1998, 2009, 2010, 2019	5
BD-19 5036	V3508 Sgr, HD 170682	1998, 2009, 2018, 2019	7
BD-12 5132	HD 172252	1998, 2018, 2019, 2020	5
BD-02 5328	HD 196712	1998, 2009, 2010, 2013, 2018, 2019, 2022	12
BD-01 3834	HD 187350	1998, 2009, 2010, 2018, 2019, 2020, 2022	11
BD-00 3543	HD 173371	1998, 2009, 2010, 2018, 2019, 2020	9
BD+02 3815	HD 179343	1998, 2009, 2010, 2018, 2019, 2020	10
BD+05 3704	HD 168797	1998, 2002, 2009, 2010, 2018, 2019, 2020	10
BD+17 4087	HD 350559	1998, 2018, 2019, 2020, 2022	9
BD+19 578	13 Tau, HR 1126, HD 23016	1998, 2009, 2010, 2013, 2017, 2018, 2019, 2020, 2022	13
BD+20 4449	HD 191531	1998, 2009, 2010, 2022	5
BD+21 4695	25 Peg, HD 210129	1998, 2009, 2010, 2013, 2018, 2020, 2022	9
BD+23 1148	HD 250289	1998, 2009, 2010, 2013, 2018, 2019, 2020, 2021, 2022	12
BD+25 4083	HD 339483	1998, 2009, 2010, 2018, 2019, 2020, 2022	12
BD+27 797	HD 244894	1998, 2009, 2010, 2013, 2018, 2019, 2022	19
BD+27 850	HD 246878	1998, 2009, 2010, 2013, 2018, 2020, 2021, 2022	12
BD+27 3411	β 2 Cyg, HR 7418, HD 183914	1998, 2002, 2009, 2010, 2018, 2019, 2020, 2022	12
BD+28 3598	HD 333452	1998, 2009, 2010, 2018, 2019, 2020, 2022	7
BD+29 3842	HD 333226	1998, 2009, 2010, 2018, 2019, 2020, 2022	9
BD+29 4453	HD 205618	1998, 2009, 2010, 2013, 2018, 2019, 2020, 2022	12
BD+30 3227	HR 6971, HD 171406	1998, 2002, 2009, 2010, 2018, 2019, 2020, 2021, 2022	13
BD+31 4018	V2113 Cyg, HD 193009	1998, 2009, 2010, 2013, 2018, 2019, 2020, 2022	13
BD+36 3946	HD 228438	1998, 2002, 2009, 2010, 2013, 2018, 2019, 2020, 2022	15
BD+37 675	HR 894, HD 18552	1998, 2009, 2010, 2013, 2018, 2019, 2020, 2022	10
BD+37 3856	HD 228650	1998, 2009, 2010, 2013, 2018, 2019, 2020, 2022	14
BD+40 1213	HD 33604	1998, 2009, 2010, 2013, 2018, 2019, 2020, 2021, 2022	14
BD+42 1376	V434 Aur, HD 37657	1998, 2009, 2010, 2013, 2018, 2019, 2020, 2021, 2022	13
BD+42 4538	HD 216581	1998, 2002, 2009, 2010, 2013, 2018, 2019, 2020, 2022	12
BD+43 1048	HD 276738	1998, 2009, 2010, 2013, 2018, 2019, 2022	11
BD+45 933	HD 27846	1998, 2009, 2010, 2013, 2018, 2019, 2020, 2022	13
BD+45 3879	HD 211835	1998, 2002, 2009, 2010, 2013, 2018, 2019, 2020, 2022	12
BD+46 275	φ And, HR 335, HD 6811	1998, 2009, 2010, 2013, 2018, 2019, 2020, 2022	15
BD+47 183	22 Cas, HR 193, HD 4180	1998, 2009, 2010, 2013, 2018, 2019, 2020, 2022	14
BD+47 857	ψ Per, HR 1087, HD 22192	1998, 2009, 2010, 2013, 2017, 2018, 2019, 2020, 2022	13
BD+47 939	48 Per, HR 1273, HD 25940	1998, 2001, 2009, 2010, 2013, 2017, 2018, 2019, 2020, 2022	15
BD+47 3985	EW Lac, HR 8731, HD 217050	1998, 2002, 2005, 2017, 2018, 2019, 2020, 2022	12
BD+49 614	HD 13867	1998, 2009, 2010, 2013, 2018, 2022	9
BD+50 825	HR 1160, HD 23552	1998, 2007, 2009, 2010, 2013, 2018, 2019, 2020, 2021, 2022	15
BD+50 3430	HD 207232	1998, 2009, 2010, 2013, 2018, 2019, 2020, 2022	15
BD+51 3091	HR 8259, HD 20551	1998, 2009, 2010, 2013, 2018, 2019, 2022	12
BD+53 2599	HD 203356	1998, 2009, 2010, 2013, 2018, 2019, 2020, 2022	14
BD+55 552	HD 13669	1998, 2009, 2010, 2013, 2018, 2019, 2022	12
BD+55 605	V361 Per, HD 14605	1998, 2009, 2010, 2013, 2018, 2022	8
BD+55 2411	HD 195554	1998, 2002, 2009, 2010, 2013, 2018, 2019, 2020, 2022	17
BD+56 473	V356 Per	1998, 2009, 2010, 2013, 2018, 2022	7
BD+56 478	V358 Per, HD 13890	1998, 2002, 2009, 2010, 2013, 2018, 2019, 2020, 2022	10
BD+56 484	V502 Per	1998, 2009, 2010, 2013, 2018, 2020, 2022	12
BD+56 493	-	1998, 2009, 2010, 2013, 2018, 2019, 2022	9
BD+56 511	-	1998, 2009, 2010, 2013, 2018, 2019, 2021, 2022	11
BD+56 573	-	1998, 2009, 2010, 2013, 2018, 2019, 2022	12
BD+57 681	HD 237056	1998, 2009, 2010, 2013, 2018, 2019, 2020, 2022	13
BD+58 554	HD 237060	1998, 2009, 2010, 2013, 2018, 2019, 2020, 2022	12
BD+58 2320	HD 239758	1998, 2009, 2010, 2013, 2018, 2019, 2020, 2022	12

Table A2. The list of objects, including the spectral and luminosity classes, distances, theoretical luminosities, masses and radius of the star, theoretical critical velocity and reddening. \dagger indicates that the distances are from the Hipparcos catalog instead of Gaia. All the theoretical $\log(L/L_\odot)$ values come from [de Jager & Nieuwenhuijzen \(1987\)](#) and they only depend on the spectral type, while the M/M_\odot , R/R_\odot and v_{crit} are derived from equations 3, 4, 5 and 6. The values of the reddening $E(B - V)$ come from [Howells et al. \(2001\)](#).

Object	Spectral Type	d (pc)	$\log(L/L_\odot)$	M/M_\odot	R/R_\odot	v_{crit} (km/s)	$E(B - V)$
CD-28 14778	B2III	1624 ± 73	4.047	10.638	5.490	496.1	0.54
CD-27 11872	B0.5V-III	1270 ± 38	4.258	12.604	5.855	522.9	0.86
CD-27 16010	B8IV	168.9 ± 8.4	2.337	3.678	2.844	405.3	0.16
CD-25 12642	B0.7III	1414 ± 39	5.034	23.517	7.983	611.7	-
CD-22 13183	B7V	882 ± 38	2.203	3.403	2.719	398.7	0.27
BD-20 5381	B5V	643 ± 16	2.681	4.491	3.220	420.9	-
BD-19 5036	B4III	667 ± 16	3.562	7.204	4.889	432.6	0.51
BD-12 5132	BN0.2III	1630 ± 190	4.846	20.219	7.328	592.0	0.78
BD-02 5328	B7V	350.4 ± 6.6	2.203	3.403	2.719	398.7	-0.06
BD-01 3834	B2IV	2010 ± 110	3.84	9.008	5.197	469.2	0.08
BD-00 3543	B7V	287.1 ± 3.0	2.203	3.403	2.719	398.7	0.06
BD+02 3815	B7-8sh	$790 \pm 510^\dagger$	2.094	3.195	2.624	393.2	-0.03
BD+05 3704	B2.5V	418.8 ± 7.7	3.332	6.554	4.206	444.9	-0.13
BD+17 4087	B6III-V	2096 ± 64	2.758	4.697	3.316	424.1	0.08
BD+19 578	B8V	159.3 ± 2.1	1.985	2.999	2.536	387.6	-
BD+20 4449	B0III	2130 ± 180	4.928	21.596	7.600	600.8	0.16
BD+21 4695	B6III-V	204.5 ± 3.7	3.08	5.662	3.774	436.5	0.03
BD+23 1148	B2III	2180 ± 130	4.047	10.638	5.490	496.1	0.89
BD+25 4083	B0.7-1III	1269 ± 22	4.573	16.236	6.549	561.1	-
BD+27 797	B0.5V	1977 ± 58	4.258	12.604	5.855	522.9	1.59
BD+27 850	B1.5IV	1231 ± 29	4.081	10.933	5.544	500.4	0.65
BD+27 3411	B8V	122.1 ± 1.2	1.985	2.999	2.536	387.6	-0.18
BD+28 3598	BO9II	2295 ± 71	5.516	34.643	10.253	655.1	1.18
BD+29 3842	B1II	4560 ± 250	4.93	21.631	7.607	601.0	0.73
BD+29 4453	B1.5V	1224 ± 48	3.733	8.266	5.067	455.2	0.11
BD+30 3227	B4V	364.5 ± 9.1	2.936	5.208	3.557	431.2	0.12
BD+31 4018	B1.5V	885 ± 18	3.733	8.266	5.067	455.2	-0.36
BD+36 3946	B1V	2350 ± 140	3.998	10.228	5.415	489.8	0.58
BD+37 675	B7V	224.1 ± 2.8	2.203	3.403	2.719	398.7	0.13
BD+37 3856	B0.5V	2195 ± 56	4.258	12.604	5.855	522.9	1.11
BD+40 1213	B2.5IV	1102 ± 33	3.716	8.153	5.048	452.9	0.17
BD+42 1376	B2V	698 ± 16	3.465	6.670	4.798	420.2	0.31
BD+42 4538	B2.5V	594.6 ± 9.9	3.332	6.553	4.206	444.9	0.27
BD+43 1048	B6IIish	971 ± 27	3.08	5.662	3.774	436.5	0.39
BD+45 933	B1.5V	957 ± 26	3.733	8.266	5.067	455.2	0.51
BD+45 3879	B1.5V	1876 ± 73	3.733	8.266	5.067	455.2	-
BD+46 275	B5III	$220 \pm 29^\dagger$	3.319	6.504	4.182	444.5	0.2
BD+47 183	B2.5V	$216 \pm 18^\dagger$	3.332	6.554	4.206	444.9	0.19
BD+47 857	B4V-III	167.7 ± 3.7	2.936	5.208	3.557	431.2	0.37
BD+47 939	B2.5V	156.8 ± 7.2	3.332	6.554	4.206	444.9	0.41
BD+47 3985	B1.5V	287.4 ± 5.8	3.733	8.266	5.067	455.2	0.32
BD+49 614	B5III	499 ± 86	3.319	6.504	4.182	444.5	0.23
BD+50 825	B7V	249.8 ± 2.1	2.203	3.403	2.719	398.7	0.46
BD+50 3430	B8V	384.8 ± 4.4	1.985	2.999	2.536	387.6	0.07
BD+51 3091	B7III	457.7 ± 6.3	2.576	4.226	3.096	416.3	0.13
BD+53 2599	B8V	637 ± 23	1.985	2.999	2.536	387.6	-
BD+55 552	B4V	699 ± 11	2.936	5.208	3.557	431.2	0.07
BD+55 605	B1V	2311 ± 84	3.998	10.227	5.415	489.8	0.78
BD+55 2411	B8.5V	305.7 ± 9.2	1.884	2.828	2.459	382.2	0.27
BD+56 473	B1V-III	2460 ± 98	3.998	10.228	5.415	489.8	0.57
BD+56 478	B1.5V	2100 ± 230	3.733	8.266	5.067	455.2	0.6
BD+56 484	B1V	2381 ± 90	3.998	10.228	5.415	489.8	0.78
BD+56 493	B1V	2850 ± 160	3.998	10.228	5.415	489.8	0.57
BD+56 511	B1III	2590 ± 120	4.508	15.409	6.389	553.5	0.72
BD+56 573	B1.5V	2200 ± 120	3.733	8.266	5.067	455.2	0.89
BD+57 681	B0.5V	1132 ± 33	4.258	12.604	5.855	522.9	1.17
BD+58 554	B7V	662.2 ± 6.9	2.203	3.403	2.719	398.7	0.27
BD+58 2320	B2V	1254 ± 24	3.465	6.670	4.798	420.2	0.62

Table A3. The list of objects, with the calculated polarization degrees for each BVR band, and the weighted polarization average of them, for the Oct 2022 observations. The errors quoted in this table have been calculated only from photon counting statistics and do not include the MOPTOP systematic errors of ~ 0.002 . Because the error from the calculations is smaller than the systematic error, the final value of the error for the average polarization degree is $S(\bar{P}) = 0.002$. Final polarization measurements incorporating the systematic error and the effect of interstellar polarization are given in Table A7.

Object	P_V	$S(P_V)$	P_B	$S(P_B)$	P_R	$S(P_R)$	\bar{P}
CD-28 14778	0.03467	$6 \cdot 10^{-5}$	0.0367	0.0001	0.02589	$3 \cdot 10^{-5}$	0.032
CD-27 11872	0.07152	$3 \cdot 10^{-5}$	0.07755	$6 \cdot 10^{-5}$	0.06398	$2 \cdot 10^{-5}$	0.071
CD-27 16010	0.0035203	$8 \cdot 10^{-7}$	0.005	0.003	0.0025063	$3 \cdot 10^{-7}$	0.004
CD-25 12642	0.03264	$5 \cdot 10^{-5}$	0.0420	0.0001	0.02167	$3 \cdot 10^{-5}$	0.032
CD-22 13183	0.010014	$9 \cdot 10^{-6}$	0.0142	0.0002	0.01086	$2 \cdot 10^{-5}$	0.012
BD-20 5381	0.0162	0.0001	0.0122	0.0004	0.00977	$3 \cdot 10^{-5}$	0.013
BD-19 5036	0.006470	$2 \cdot 10^{-6}$	0.0442	$4 \cdot 10^{-5}$	0.03798	$1 \cdot 10^{-5}$	0.029
BD-12 5132	0.106	0.001	0.106	0.001	0.064	0.001	0.091
BD-02 5328	0.003889	$3 \cdot 10^{-6}$	0.0046	0.0003	0.0036205	$9 \cdot 10^{-7}$	0.004
BD-01 3834	0.003	0.001	0.0040	0.0003	0.00516	$6 \cdot 10^{-5}$	0.004
BD-00 3543	0.008073	$6 \cdot 10^{-6}$	0.008	0.005	0.006470	$2 \cdot 10^{-6}$	0.007
BD+02 3815	0.010120	$8 \cdot 10^{-6}$	0.01210	$2 \cdot 10^{-5}$	0.007586	$3 \cdot 10^{-6}$	0.010
BD+05 3704	0.005612	$1 \cdot 10^{-6}$	0.00922	$8 \cdot 10^{-6}$	0.030378	$6 \cdot 10^{-6}$	0.014
BD+17 4087	0.0221	0.0003	0.02	0.02	0.0206	0.0002	0.022
BD+19 578	0.004838	$1 \cdot 10^{-6}$	0.0055	0.0001	0.0046032	$7 \cdot 10^{-7}$	0.005
BD+20 4449	0.01052	$2 \cdot 10^{-5}$	0.01025	$8 \cdot 10^{-5}$	0.007306	$9 \cdot 10^{-6}$	0.009
BD+21 4695	0.002800	$3 \cdot 10^{-6}$	0.004	0.004	0.001353	$1 \cdot 10^{-6}$	0.002
BD+23 1148	0.03	0.08	0.0316	0.0003	0.0311	0.0009	0.032
BD+25 4083	0.016	0.001	0.02	0.01	0.02	0.06	0.016
BD+27 797	0.02	0.03	-	-	0.02	0.01	0.017
BD+27 850	0.0099	0.0001	0.010	0.001	0.00595	$5 \cdot 10^{-5}$	0.009
BD+27 3411	0.0040326	$7 \cdot 10^{-7}$	0.005223	$2 \cdot 10^{-6}$	0.020104	$1 \cdot 10^{-6}$	0.010
BD+28 3598	0.0538	0.0002	0.0633	0.0003	0.037	0.009	0.051
BD+29 3842	0.0167	0.0001	0.0202	0.0004	0.01389	$5 \cdot 10^{-5}$	0.017
BD+29 4453	0.01030	$3 \cdot 10^{-5}$	0.0104	0.0002	0.00929	$1 \cdot 10^{-5}$	0.010
BD+30 3227	0.01325	$1 \cdot 10^{-5}$	0.0247	0.0004	0.009893	$7 \cdot 10^{-6}$	0.016
BD+31 4018	0.0140	0.0009	0.01481	$4 \cdot 10^{-5}$	0.01329	$2 \cdot 10^{-5}$	0.014
BD+36 3946	0.00725	$5 \cdot 10^{-5}$	0.0062	0.0002	0.00746	$1 \cdot 10^{-5}$	0.007
BD+37 675	0.00427	$2 \cdot 10^{-5}$	0.00553	$4 \cdot 10^{-5}$	0.004496	$6 \cdot 10^{-6}$	0.005
BD+37 3856	0.0154	0.0001	0.0124	0.0005	0.01304	$7 \cdot 10^{-5}$	0.014
BD+40 1213	0.016	0.006	0.015	0.002	0.0146	0.0002	0.015
BD+42 1376	0.0156	0.0002	0.02	0.01	0.02	0.02	0.015
BD+42 4538	0.00922	$3 \cdot 10^{-5}$	0.0093	0.0003	0.00704	$2 \cdot 10^{-5}$	0.008
BD+43 1048	0.027	0.004	0.024	0.003	0.024	0.002	0.025
BD+45 933	0.0229	0.0001	0.02446	$8 \cdot 10^{-5}$	0.0230	0.0002	0.023
BD+45 3879	0.00539	$3 \cdot 10^{-5}$	0.0064	0.0002	0.00665	$1 \cdot 10^{-5}$	0.006
BD+46 275	0.009412	$1 \cdot 10^{-6}$	0.00966	$3 \cdot 10^{-5}$	0.0089211	$6 \cdot 10^{-7}$	0.009
BD+47 183	0.011340	$1 \cdot 10^{-6}$	0.010746	$3 \cdot 10^{-6}$	0.0098539	$7 \cdot 10^{-7}$	0.011
BD+47 857	0.0045151	$4 \cdot 10^{-7}$	0.00568	$3 \cdot 10^{-5}$	0.0032336	$1 \cdot 10^{-7}$	0.002
BD+47 939	0.0115475	$3 \cdot 10^{-7}$	0.0120	0.0002	0.0109207	$1 \cdot 10^{-7}$	0.011
BD+47 3985	0.004066	$2 \cdot 10^{-6}$	0.004237	$5 \cdot 10^{-6}$	0.0024482	$8 \cdot 10^{-7}$	0.004
BD+49 614	0.01308	$5 \cdot 10^{-5}$	0.01	0.14	0.01148	$2 \cdot 10^{-5}$	0.012
BD+50 825	0.006995	$2 \cdot 10^{-6}$	0.00843	$4 \cdot 10^{-5}$	0.006553	$1 \cdot 10^{-6}$	0.007
BD+50 3430	0.00559	$1 \cdot 10^{-5}$	0.01	0.01	0.004803	$4 \cdot 10^{-6}$	0.005
BD+51 3091	0.007973	$6 \cdot 10^{-6}$	0.00772	$2 \cdot 10^{-5}$	0.006755	$3 \cdot 10^{-6}$	0.007
BD+53 2599	0.00668	$4 \cdot 10^{-5}$	0.007	0.002	0.00465	$2 \cdot 10^{-5}$	0.006
BD+55 552	0.03	0.01	0.0297	0.0004	0.02	0.01	0.027
BD+55 605	0.04	0.01	0.0460	0.0006	0.04	0.02	0.042
BD+55 2411	0.001685	$6 \cdot 10^{-6}$	0.00424	$4 \cdot 10^{-5}$	0.001212	$2 \cdot 10^{-6}$	0.002
BD+56 473	0.0485	0.0006	0.0501	0.0002	0.043	0.008	0.047
BD+56 478	0.0386	0.0007	0.0392	0.0002	0.03	0.03	0.037
BD+56 484	-	-	0.0417	0.0006	0.0327	0.0006	0.037
BD+56 493	0.046	0.008	0.0475	0.0005	0.040	0.002	0.044
BD+56 511	0.041	0.001	0.0437	0.0003	0.04	0.14	0.041
BD+56 573	0.04	0.03	0.0475	0.0006	0.036	0.003	0.042
BD+57 681	0.05971	$2 \cdot 10^{-5}$	0.06348	$6 \cdot 10^{-5}$	0.05678	$1 \cdot 10^{-5}$	0.060
BD+58 554	0.0325	0.0002	0.0346	0.0002	0.032	0.001	0.033
BD+58 2320	0.0201	0.0007	0.02	0.04	0.0162	0.0002	0.017

Table A4. The list of objects, with the calculated polarization angles for each BVR band, and the weighted polarization angle average of them, for the Oct 2022 observations. The angle values are between 0 and 180°. The errors quoted in this table have been calculated only from photon counting statistics and do not include the MOPTOP systematic errors of $\sim 1^\circ$. Because the error from the calculations is smaller than the systematic error, the final value of the error for the average polarization degree is $S(\bar{\theta}) = 1^\circ$. Final polarization measurements incorporating the systematic error and the effect of interstellar polarization are given in Table A7.

Object	θ_V	$S(\theta_V)$	θ_B	$S(\theta_B)$	θ_R	$S(\theta_R)$	$\bar{\theta}$
CD-28 14778	184.97	0.04	184.93	0.07	181.62	0.02	4
CD-27 11872	169.86	0.01	170.67	0.03	170.052	0.009	170
CD-27 16010	172.87	0.05	164	7	172.89	0.02	169
CD-25 12642	191.84	0.03	193.46	0.05	196.29	0.03	14
CD-22 13183	174.011	0.005	179.9	0.1	169.74	0.04	175
BD-20 5381	182.2	0.2	177.2	0.6	177.41	0.06	179
BD-19 5036	176.200	0.003	190.06	0.02	191.528	0.007	10
BD-12 5132	169.07	0.03	169.07	0.02	162.5	0.1	168
BD-02 5328	257.16	0.02	284	53	268.998	0.002	91
BD-01 3834	268	191	163	18	260.9	0.4	80
BD-00 3543	185.47	0.02	186	3	176.200	0.003	3
BD+02 3815	179.84	0.03	180.23	0.08	178.28	0.01	0
BD+05 3704	281.803	0.003	286.00	0.01	218.018	0.005	30
BD+17 4087	186	3	189	1231	188	5	8
BD+19 578	259.407	0.004	275	2	265.906	0.002	87
BD+20 4449	190.21	0.08	191.0	0.4	188.05	0.02	10
BD+21 4695	157.5	0.3	134	47	149.57	0.09	155
BD+23 1148	162	62	164.8	0.2	164.0	0.5	164
BD+25 4083	345	3	259	27	343	63	166
BD+27 797	187	25	-	-	189	17	8
BD+27 850	147.1	0.9	155	4	142.1	0.4	149
BD+27 3411	331.280	0.006	246.54	0.02	332.0686	0.0007	153
BD+28 3598	218.73	0.05	219.54	0.08	221	3	40
BD+29 3842	260.6	0.2	260.5	0.5	259.00	0.07	80
BD+29 4453	39.14	0.02	39.4	0.2	38.94	0.01	39
BD+30 3227	244.82	0.02	334.8	0.4	246.98	0.02	65
BD+31 4018	259.1	0.8	261.90	0.03	257.30	0.02	80
BD+36 3946	266	2	257	6	342.77	0.06	168
BD+37 675	144.2	0.3	149	2	148.33	0.05	147
BD+37 3856	307.5	0.2	306.0	0.8	307.6	0.1	127
BD+40 1213	162	5	166	2	166.9	0.4	165
BD+42 1376	172.6	0.4	176	19	176	51	175
BD+42 4538	81.7	0.2	92	1	83.0	0.1	86
BD+43 1048	356	1	90.7	0.4	178	2	88
BD+45 933	318.1	0.4	318.8	0.4	318	1	138
BD+45 3879	27.0	0.2	21.7	0.8	25.12	0.03	24
BD+46 275	85.205	0.002	91.30	0.02	90.0299	0.0009	89
BD+47 183	81.48	0.02	81.8	0.6	82.590	0.009	82
BD+47 857	38.778	0.001	54.9	0.3	47.7664	0.0004	64
BD+47 939	354.3414	0.0003	175.51	0.04	352.6755	0.0001	174
BD+47 3985	58.11	0.06	44.23	0.06	55.27	0.04	53
BD+49 614	102.87	0.03	106	25	103.123	0.007	104
BD+50 825	326.338	0.002	328.02	0.05	322.430	0.001	146
BD+50 3430	189.9	0.1	191	19	9.62	0.02	10
BD+51 3091	24.57	0.07	22.3	0.6	19.93	0.02	22
BD+53 2599	37.3	0.6	113	52	40.5	0.3	33
BD+55 552	110	9	114.3	0.4	110	3	112
BD+55 605	119	15	123.6	0.8	119	13	121
BD+55 2411	141.5	0.2	146.8	0.4	310.8	0.3	149
BD+56 473	108.0	0.1	110.50	0.05	109	1	109
BD+56 478	110.7	0.4	114.0	0.1	111	13	112
BD+56 484	-	-	126.8	0.9	123.6	0.7	124
BD+56 493	120	8	123.5	0.6	121	2	122
BD+56 511	111.8	0.4	115.8	0.1	113	36	114
BD+56 573	118	36	120.0	0.6	119	3	119
BD+57 681	307.438	0.002	309.860	0.005	307.1085	0.0005	128
BD+58 554	296.2	0.2	298.0	0.1	296.8	0.7	117
BD+58 2320	58	1	67	34	55.6	0.5	60

Table A5. Comparison of our values with the ones from [Yudin \(2001\)](#).

Object	Object (2001)	$vsini$ (2001) (km/s)	P (%) (2001)	θ (2001)	$vsini$ (2022) (km/s)	\bar{P} (2022)	$\bar{\theta}$ (2022)
CD-28 14778	HD 171757	182 ± 18	0.43 ± 0.10	36	141 ± 23	3.2	4
CD-27 11872	HD 161103	260 ± 26	4.83 ± 0.12	172	210 ± 17	7.1	170
CD-27 16010	HD 214748	222 ± 26	0.09 ± 0.10	155	189 ± 7	0.4	169
CD-22 13183	HD 172158	232 ± 26	0.54 ± 0.10	143	169 ± 79	1.2	175
BD-20 5381	HD 177015	236 ± 24	0.51 ± 0.20	0	197 ± 72	1.3	179
BD-19 5036	HD 170682	121 ± 12	-	-	126 ± 17	2.9	10
BD-12 5132	HD 172252	146 ± 15	4.65 ± 0.20	148	98 ± 11	9.1	168
BD-02 5328	HD 196712	199 ± 19	0.35 ± 0.04	95	170 ± 8	0.4	91
BD-01 3834	HD 187350	199 ± 20	0.78 ± 0.20	82	166 ± 12	0.4	80
BD-00 3543	HD 173371	291 ± 4	-	-	224 ± 15	0.7	3
BD+02 3815	HD 179343	261 ± 36	-	-	197 ± 10	1.0	0
BD+05 3704	HD 168797	251 ± 6	0.78 ± 0.20	64	211 ± 59	1.4	30
BD+17 4087	HD 350559	186 ± 19	-	-	204 ± 79	2.2	8
BD+19 578	HD 23016	278 ± 14	0.60 ± 0.04	87	215 ± 17	0.5	87
BD+20 4449	HD 191531	80 ± 3	-	-	90 ± 43	0.9	10
BD+21 4695	HD 210129	201 ± 32	0.28 ± 0.04	7	157 ± 17	0.2	155
BD+23 1148	HD 250289	125 ± 13	2.95 ± 0.18	162	87 ± 77	3.2	164
BD+27 797	HD 244894	177 ± 18	1.61 ± 0.18	19	197 ± 18	1.7	8
BD+27 850	HD 246878	137 ± 14	0.55 ± 0.18	133	121 ± 18	0.9	149
BD+27 3411	HD 183914	220 ± 25	-	-	170 ± 13	1.0	153
BD+29 4453	HD 205618	299 ± 65	1.24 ± 0.20	26	247 ± 26	1.0	39
BD+30 3227	HD 171406	264 ± 10	0.28 ± 0.20	13	208 ± 8	1.6	65
BD+31 4018	HD 193009	220 ± 26	0.65 ± 0.20	75	225 ± 30	1.4	80
BD+36 3946	HD 228438	219 ± 22	1.15 ± 0.20	170	178 ± 23	0.7	168
BD+37 675	HD 18552	260 ± 12	-	-	223 ± 21	0.5	147
BD+40 1213	HD 33604	134 ± 20	1.29 ± 0.20	168	122 ± 7	1.5	165
BD+42 1376	HD 37657	216 ± 20	1.66 ± 0.20	174	196 ± 10	1.5	175
BD+42 4538	HD 216581	282 ± 28	-	-	236 ± 30	0.8	86
BD+43 1048	HD 276738	220 ± 22	-	-	205 ± 46	2.5	88
BD+45 933	HD 27846	134 ± 15	-	-	135 ± 14	2.3	138
BD+45 3879	HD 211835	207 ± 15	-	-	186 ± 10	0.6	24
BD+46 275	HD 6811	88 ± 13	0.74 ± 0.12	90	111 ± 20	0.9	89
BD+47 183	HD 4180	221 ± 9	0.70 ± 0.13	85	167 ± 12	1.1	82
BD+47 857	HD 22192	297 ± 41	0.80 ± 0.15	45	227 ± 12	0.2	64
BD+47 939	HD 25940	198 ± 31	0.25 ± 0.10	145	153 ± 8	1.1	174
BD+47 3985	HD 217050	301 ± 16	1.55 ± 0.20	75	232 ± 14	0.4	53
BD+49 614	HD 13867	93 ± 16	-	-	135 ± 114	1.2	104
BD+50 825	HD 23552	218 ± 3	0.55 ± 0.05	140	184 ± 11	0.7	146
BD+50 3430	HD 207232	281 ± 28	-	-	198 ± 19	0.5	10
BD+55 552	HD 13669	304 ± 22	-	-	243 ± 29	2.7	112
BD+55 605	HD 14605	150 ± 3	3.78 ± 0.20	118	142 ± 25	4.2	121
BD+55 2411	HD 195554	215 ± 21	-	-	193 ± 9	0.2	149
BD+56 473	V356 Per	258 ± 26	4.38 ± 0.18	111	218 ± 23	4.7	109
BD+56 478	HD 13890	179 ± 8	3.46 ± 0.18	107	152 ± 30	3.7	112
BD+56 484	V502 Per	228 ± 24	3.46 ± 0.18	124	182 ± 39	3.7	124
BD+56 493	BD+56 493	311 ± 31	3.64 ± 0.18	126	175 ± 41	4.4	122
BD+56 511	BD+56 511	111 ± 11	-	-	108 ± 54	4.1	114
BD+56 573	BD+56 573	335 ± 34	-	-	210 ± 51	4.2	119
BD+57 681	HD 237056	160 ± 17	5.90 ± 0.18	125	155 ± 20	6.0	128
BD+58 2320	HD 239758	281 ± 28	2.12 ± 0.18	59	244 ± 39	1.7	60

Table A6. The distance D to the object, and the minimum and maximum distance (d) that we take. The stars included in this range are used for our linear fits to obtain an estimation of the interstellar polarization. The large variation in these ranges is due to two main reasons: loss of linearity at big distances away from the star, or lack of data covering any other suitable range.

Object	D (pc)	S(D) (pc)	Min d (pc)	Max d (pc)
CD-28 14778	1625	73	78	4926
CD-27 11872	1270	38	93	3657
CD-27 16010	168.9	8.4	50.4	1268.6
CD-25 12642	1414	39	698	2395
CD-22 13183	882	38	43	997
BD-20 5381	643	16	74	4714
BD-19 5036	667	16	108	3898
BD-12 5132	1630	190	43	597
BD-02 5328	350.4	6.6	40.7	1425.2
BD-01 3834	2010	110	49	1822
BD-00 3543	287.1	3	42.5	4714.2
BD+02 3815	790	510	132	2700
BD+05 3704	418.8	7.7	46.3	779.9
BD+17 4087	2096	64	131	3986
BD+19 578	159.3	2.1	145.7	4405.5
BD+20 4449	2130	180	131	381
BD+21 4695	204.5	3.7	46.8	434.4
BD+23 1148	2180	130	50	1263
BD+25 4083	1269	22	93	4693
BD+27 797	1977	58	854	3344
BD+27 850	1231	29	54	374
BD+27 3411	122.1	1.2	163.4	350.4
BD+28 3598	2295	71	72	3527
BD+29 3842	4560	250	126	1753
BD+29 4453	1224	48	13	201
BD+30 3227	364.5	9.1	43.4	597.3
BD+31 4018	885	18	2005	3455
BD+36 3946	2350	140	2005	3779
BD+37 675	224.1	2.8	46.4	2005.2
BD+37 3856	2195	56	126	4464
BD+40 1213	1102	33	107	2449
BD+42 1376	698	16	2007	4924
BD+42 4538	594.6	9.9	37	963.7
BD+43 1048	971	27	115	1879
BD+45 933	957	26	2005	3346
BD+45 3879	1876	73	51	1910
BD+46 275	220	29	79	4446
BD+47 183	216	18	102	162
BD+47 857	167.7	3.7	147.6	4926.9
BD+47 939	156.8	7.2	27.6	1224
BD+47 3985	287.4	5.8	53.7	406.2
BD+49 614	499	86	56	4578
BD+50 825	249.8	2.1	2005.3	3455.3
BD+50 3430	384.8	4.4	31.8	583.7
BD+51 3091	457.7	6.3	24.5	582.2
BD+53 2599	637	23	127	4254
BD+55 552	699	11	43	3812
BD+55 605	2311	84	101	4446
BD+55 2411	305.7	9.2	111.2	515.9
BD+56 473	2460	98	44	515
BD+56 478	2100	230	38	964
BD+56 484	2381	90	62	698
BD+56 493	2850	160	28	96
BD+56 511	2590	120	41	800
BD+56 573	2200	120	2005	3963
BD+57 681	1132	33	1527	4945
BD+58 554	662.2	6.9	38.1	963.7
BD+58 2320	1254	24	74	4714

Table A7. The calculated values for the interstellar and intrinsic polarization degrees and angles. The estimated systematic error from MOPTOP is $S(\bar{P}) = 0.002$ and $S(\bar{\theta}) = 1$ degree. The error of the interstellar polarization values has been obtained from the linear fit to nearby stars, while the error of the intrinsic polarization values has been obtained from the calculations of q_{in} and u_{in} and the following derivation of P_{in} and θ_{in} .

Object	\bar{P}	$\bar{\theta}$	P_{is}	$S(P_{is})$	θ_{is}	$S(\theta_{is})$	P_{in}	$S(P_{in})$	θ_{in}	$S(\theta_{in})$
CD-28 14778	0.032	4	0.0063	0.0005	23.72	0.05	0.01	0.01	171	3
CD-27 11872	0.071	170	0.019	0.001	24.54	0.03	0.010	0.02	145.7	0.5
CD-27 16010	0.004	169	0.0195	0.0005	34.92	0.01	0.015	0.005	16.7	0.3
CD-25 12642	0.032	14	0.013	0.001	29.66	0.04	0.020	0.04	166	2
CD-22 13183	0.012	175	0.0277	0.0009	23.17	0.02	0.001	0.007	141.6	0.9
BD-20 5381	0.013	179	0.0079	0.0005	31.15	0.02	0.010	0.004	1	4
BD-19 5036	0.029	10	0.00072	0.00005	42.312	0.004	0.009	0.005	25.9	0.3
BD-12 5132	0.091	168	0.0044	0.0001	24.95	0.02	0.006	0.005	28.6	0.4
BD-02 5328	0.004	91	0.0069	0.0004	34.24	0.01	0.011	0.005	176	2
BD-01 3834	0.004	80	0.020	0.001	23.58	0.03	0.01	0.01	132.8	0.1
BD-00 3543	0.007	3	0.029	0.003	28.85	0.04	0.02	0.02	135.45	0.01
BD+02 3815	0.010	0	0.011	0.002	35.72	0.05	0.01	0.01	150.9	0.7
BD+05 3704	0.014	30	0.0065	0.0003	27.88	0.02	0.007	0.005	31.9	0.2
BD+17 4087	0.022	8	0.00094	0.00009	44.8314	0.0004	0.071	0.007	9.6	0.2
BD+19 578	0.005	87	0.00083	0.00007	44.7854	0.0004	0.032	0.006	13.3	0.3
BD+20 4449	0.009	10	0.002	0.002	20.6	0.7	0.014	0.006	25.6	0.2
BD+21 4695	0.002	155	0.001	0.002	27	1	0.001	0.005	34	1
BD+23 1148	0.032	164	0.032	0.002	35.26	0.01	0.029	0.005	41.04	0.02
BD+25 4083	0.016	166	0.0101	0.0005	19.86	0.04	0.004	0.004	78	1
BD+27 797	0.017	8	0.006	0.005	26.7	0.5	0.01	0.07	163	9
BD+27 850	0.009	149	0.004	0.001	5.1	0.8	0.01	0.01	178	23
BD+27 3411	0.010	153	0.007	0.001	7.9	0.4	0.00	0.09	107	32
BD+28 3598	0.051	40	0.030	0.002	12.86	0.06	0.01	0.02	114	1
BD+29 3842	0.017	80	0.0038	0.0002	3.9	0.2	0.00	0.01	26	5
BD+29 4453	0.010	39	0.001	0.002	30.4	0.8	0.004	0.006	8	4
BD+30 3227	0.016	65	0.0068	0.0005	21.78	0.05	0.00	0.01	125	1
BD+31 4018	0.014	80	0.039	0.006	20.5	0.1	0.003	0.008	86	10
BD+36 3946	0.007	168	0.052	0.004	20.11	0.06	0.021	0.006	81.8	0.5
BD+37 675	0.005	147	0.12	0.01	4.6	0.3	0.12	0.01	94.4	0.4
BD+37 3856	0.014	127	0.011	0.001	9.8	0.2	0.007	0.007	100	2
BD+40 1213	0.015	165	0.008	0.003	17.2	0.3	0.00	0.01	114	2
BD+42 1376	0.015	175	0.014	0.001	27.40	0.04	0.01	0.01	129.9	0.2
BD+42 4538	0.008	86	0.0043	0.0002	5.2	0.1	0.003	0.004	83	3
BD+43 1048	0.025	88	0.023	0.002	22.48	0.05	0.015	0.004	77.2	0.3
BD+45 933	0.023	138	0.042	0.002	20.75	0.03	0.015	0.005	71.4	0.3
BD+45 3879	0.006	24	0.0074	0.0006	3.6	0.3	0.007	0.004	68.7	0.4
BD+46 275	0.009	89	0.0021	0.0001	4.8	0.2	0.027	0.007	10.4	0.4
BD+47 183	0.011	82	0.0043	0.0003	36.82	0.01	0.01	0.04	158	5
BD+47 857	0.002	64	0.0050	0.0006	29.39	0.05	0.01	0.06	170	10
BD+47 939	0.011	174	0.007	0.001	29.36	0.07	0.004	0.004	54.0	0.2
BD+47 3985	0.004	53	0.0039	0.0008	5.1	0.6	0.007	0.008	10	2
BD+49 614	0.012	104	0.014	0.002	23.4	0.1	0.078	0.007	9.9	0.1
BD+50 825	0.007	146	0.041	0.003	20.41	0.05	0.012	0.006	68.3	0.3
BD+50 3430	0.005	10	0.005	0.001	13.5	0.2	0.004	0.004	79	1
BD+51 3091	0.007	22	0.0020	0.0003	20.91	0.09	0.003	0.004	49.9	0.2
BD+53 2599	0.006	33	0.023	0.002	17.83	0.07	0.010	0.006	11.7	0.9
BD+55 552	0.027	112	0.009	0.001	36.84	0.03	0.004	0.006	144.5	0.3
BD+55 605	0.042	121	0.0013	0.0002	28.49	0.06	0.031	0.006	3	1
BD+55 2411	0.002	149	0.0009	0.0001	20.29	0.07	0.001	0.006	29	2
BD+56 473	0.047	109	0.009	0.003	26.5	0.1	0.005	0.006	171	2
BD+56 478	0.037	112	0.0032	0.0002	10.90	0.06	0.005	0.005	46.85	0.04
BD+56 484	0.037	124	0.012	0.002	12.4	0.2	0.00	0.02	164	4
BD+56 493	0.044	122	0.0024	0.0004	15.0	0.1	0.003	0.005	45.66	0.02
BD+56 511	0.041	114	0.0026	0.0001	19.27	0.04	0.01	0.01	175	8
BD+56 573	0.042	119	0.047	0.003	20.12	0.05	0.009	0.005	90.0	0.9
BD+57 681	0.060	128	0.0106	0.0005	37.25	0.01	0.007	0.005	19.3	0.5
BD+58 554	0.033	117	0.0040	0.0004	28.60	0.04	0.009	0.005	176	3
BD+58 2320	0.017	60	0.016	0.001	25.66	0.03	0.038	0.004	45.843	0.002